Relationship of tropospheric stability to climate sensitivity and Earth's observed radiation budget

Article

Accepted Version

Relationship of tropospheric stability to climate sensitivity and Earth's observed radiation budget

Paulo Ceppi[a,1] **and Jonathan M. Gregory**[b,c]

[a]Department of Meteorology, University of Reading, Reading RG6 6BB, United Kingdom; [b]NCAS-Climate, University of Reading, Reading RG6 6BB, United Kingdom; [c]Met Office Hadley Centre, Exeter EX1 3PB, United Kingdom

This manuscript was compiled on November 3, 2017

Climate feedbacks generally become smaller in magnitude over time under CO_2 forcing in coupled climate models, leading to an increase in the effective climate sensitivity, the estimated global-mean surface warming in steady state for doubled CO_2. Here we show that the evolution of climate feedbacks in models is consistent with the effect of a change in tropospheric stability, as has recently been hypothesized, and the latter is itself driven by the evolution of the pattern of sea surface temperature response. The change in climate feedback is mainly associated with a decrease in marine tropical low cloud (a more positive shortwave cloud feedback) and with a less negative lapse rate feedback, as expected from a decrease in stability. Smaller changes in surface albedo and humidity feedbacks also contribute to the overall change in feedback, but are unexplained by stability. The spatial pattern of feedback changes closely matches the pattern of stability changes, with the largest increase in feedback occurring in the tropical East Pacific. Relationships qualitatively similar to those in the models among sea surface temperature pattern, stability, and radiative budget are also found in observations on interannual time scales. Our results suggest that constraining the future evolution of sea surface temperature patterns and tropospheric stability will be necessary for constraining climate sensitivity.

climate sensitivity | climate feedbacks | clouds | satellite observations

How much Earth will warm in response to future greenhouse gas emissions is a fundamental question in climate science. Accordingly, a widely-used metric for the evaluation and comparison of climate models is the equilibrium climate sensitivity (ECS), the steady-state global-mean surface temperature change for a doubling of CO_2 concentration relative to the pre-industrial state. A common method to estimate ECS involves assuming the climate system response to a radiative forcing F to be proportional to global-mean temperature T, according to $\lambda = (N - F)/T$ where $\lambda < 0$ (1). Here N denotes the net downward radiative imbalance, $N - F$ is the radiative response, and λ is the proportionality constant between radiative response and global-mean warming. Because its value depends on climate feedback processes involving changes in the atmospheric lapse rate, water vapor concentration, cloud properties, and surface albedo with warming, the proportionality constant λ is usually referred to as the climate feedback parameter. Assuming λ stays constant in time, we may estimate ECS by extrapolating the relationship between $N - F$ and T to the temperature at which $N = 0$, i.e. radiative balance is restored: ECS $= -F/\lambda$, if F represents the forcing of a doubling of CO_2.

Although convenient, the assumption of a constant proportionality factor λ between radiative response and global-mean warming does not hold perfectly in climate models. Indeed, in most climate models λ decreases in magnitude as time passes following an increase in CO_2 concentration, leading to an increase in the "effective" climate sensitivity over time (2–13). However, the mechanisms of this evolution are currently not understood. Targeted climate model experiments have pointed to the role of evolving patterns of sea surface temperature (SST) increase in driving the evolution of climate sensitivity and feedbacks (9, 14–17), which may alternatively also be interpreted as changing patterns of ocean heat uptake (5, 18–20). Two distinct hypotheses have been proposed to link the evolution of SSTs to climate feedbacks over the course of the transient response to CO_2 forcing:

1. Feedbacks are assumed to scale linearly with *local* temperature, but are fixed in time. Global-mean feedback varies only as a result of evolving surface warming patterns, causing the spatial weighting of local feedbacks to change as time passes (7).

2. The SST evolution favors a decrease in tropospheric stability, resulting in less free-tropospheric warming per unit surface warming. This stability decrease reduces the ability of the atmosphere to cool radiatively to space from the upper troposphere (a less negative lapse rate feedback; 17), and acts to decrease low cloud cover in subsidence regions, enhancing the absorption of solar radiation (a more positive cloud feedback; 15–17). Under this hypothesis, feedbacks may vary locally in time.

Here we show that the evolution of climate feedbacks during the transient response to increased CO_2 in current coupled climate models is consistent with the effects of changes in

Significance Statement

In current climate models, the anticipated amount of warming under greenhouse gas forcing, quantified by the "effective climate sensitivity", increases as time passes. Consequently, effective climate sensitivity values inferred from the historical record may underestimate the future warming. However, the mechanisms of this increase in effective climate sensitivity are not understood, limiting our confidence in climate model projections of future climate change. Here we present observational and modeling evidence that the magnitude of effective climate sensitivity partly depends on the evolution of the vertical profile of atmospheric warming. In climate models, as the Earth warms overall, the warming becomes increasingly muted aloft, and this alters the strength of feedbacks controlling the radiative response to greenhouse gas forcing.

P.C. designed research and analyzed the data. P.C. and J.M.G. jointly wrote the paper.

The authors declare no conflict of interest.

[1]To whom correspondence should be addressed. E-mail: p.ceppi@reading.ac.uk

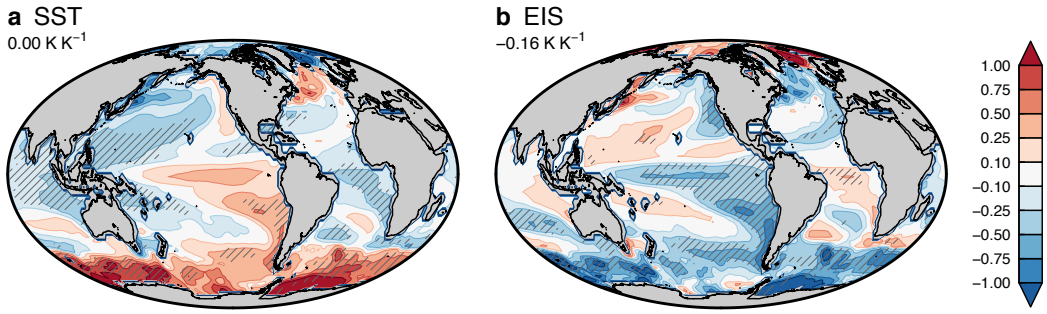

Fig. 1. Multi-model mean difference in patterns of (a) SST and (b) EIS change. The patterns of change are first calculated separately for each model for the early (years 1–20) and late (21–150) periods by regressing local annual-mean SST or EIS against global-mean annual-mean surface temperature; then the difference is calculated as late minus early period. The patterns of change in the early and late periods are shown in Fig. S1. Numbers in the top left corner of each panel denote global-mean values. Hatching denotes a multi-model mean absolute anomaly larger than one standard deviation across models.

tropospheric stability, following hypothesis 2 above. Furthermore, we demonstrate that observed interannual relationships between SST pattern, tropospheric stability, and the radiative budget qualitatively support the relationships found in climate models. Our results therefore suggest that constraining climate sensitivity will require constraints on the long-term evolution of SST and tropospheric stability.

Results

Changes in the evolution of SST and tropospheric stability. We first consider the SST evolution during the first 150 years following a quadrupling of CO_2 concentration in a set of 15 coupled climate models (Materials and Methods; Table S1). The changes over the course of the simulations are defined as the difference in responses between years 1–20 (hereafter "early period") and years 21–150 ("late period"). As the planet warms, the pattern of SST response per unit global warming evolves towards enhanced warming in the tropical East Pacific, in the Southern Ocean, in the North Atlantic, and to a lesser extent in the Northeast Pacific, while the tropical West Pacific, Northwest Pacific, tropical Atlantic, and much of the Indian Ocean experience reduced warming relative to the global average (Fig. 1a). The global-mean difference between patterns of SST change is very close to zero. (The global-mean difference between patterns of surface temperature change, including land areas, would be exactly zero by construction.) The overall spatial structure of the SST evolution is reasonably robust among models (hatching in Fig. 1a). The characteristics of the SST evolution are also similar to those found in previous studies using different sets of climate models (7, 9, 21). The delayed warming in the East Pacific and in the Southern Ocean is broadly consistent with the effects of upwelling (22, 23), but additional coupled ocean-atmosphere processes likely contribute to the evolution of the SST pattern (22, 24).

We now provide evidence that the evolution of the SST warming pattern favors a decrease in tropospheric stability. As a stability metric, we use the estimated inversion strength (EIS; 25), a measure of the strength of the inversion at the top of the boundary layer based on the difference in potential temperature between the surface and 700 hPa. EIS accounts for the temperature dependence of the moist adiabat to quantify the effective stability of the lower troposphere, and is traditionally defined over ocean regions only. In observations, EIS is strongly correlated with marine low cloud cover in subsidence regions (25), consistent with the notion that a stronger inversion is more effective at trapping moisture in the boundary layer.

How to do we expect the SST pattern to affect tropospheric stability? At any point in space, the stability change depends on the relative change in surface and free-tropospheric temperature. In the tropics, free-tropospheric temperature is largely set by the evolution of SST in warm, convective regions, such as the West Pacific warm pool, where the lapse rate is pegged to a moist adiabat owing to moist convection (26, 27). This constraint implies that the warmest regions should always remain nearly neutrally stable. Away from warm convective regions, however, the stability response will roughly depend on the ratio of local SST change to SST change in the warm pool (15). If local SST increases more than in the warm pool, stability will decrease because the free-tropospheric temperature will increase less than predicted by a local moist adiabat; the opposite would be true if local SST increased less than in the warm pool. While strictly speaking the constraint on free-tropospheric temperature applies to the tropics only, extratropical free-tropospheric temperature should be influenced by SST changes in warmer convective regions, so that a similar argument can be applied to qualitatively interpret extratropical stability changes. Although we argue that the SST pattern is the main control on the time evolution of tropospheric stability in our model simulations, additional processes can also affect stability as quantified by EIS – for example land-sea temperature contrasts and CO_2 concentrations (28).

The differences in stability response between the early and late periods in Fig. 1b are consistent with the above reasoning. The EIS difference in the warm pool around the Maritime Continent is small. Because the warm pool is warming less than average, the EIS response becomes more negative in most other regions; the larger the relative warming, the larger the stability decrease. This yields a global-mean decrease in the response of tropospheric stability to warming. It is noteworthy that the global-mean EIS response becomes more negative as time passes in all models included in this analysis (Fig. S2a).

Changes in climate feedbacks. We will now show that the evolution of climate feedbacks is consistent with the changes in

tropospheric stability over the course of the transient response to CO_2 forcing. Figure 2 shows the changes in global-mean feedback parameter decomposed into the contributions of temperature, water vapor, surface albedo, and clouds (using radiative kernels; Materials and Methods). On average, the total feedback increases by 0.50 W m^{-2} K^{-1} (−1.38 to −0.88 W m^{-2} K^{-1}), consistent with previous findings (9). Consequently, the estimated ECS increases by 0.57 K on average (2.83 to 3.40 K; Fig. S2b). The change in feedback is primarily due to the effect of clouds (0.21 W m^{-2} K^{-1}), followed by the lapse rate feedback (0.14 W m^{-2} K^{-1}), with smaller contributions of changes in surface albedo (0.09 W m^{-2} K^{-1}) and relative humidity (0.06 W m^{-2} K^{-1}). The increase in cloud feedback is almost entirely due to a change in shortwave reflection (0.20 W m^{-2} K^{-1}). Since the mean residual is near zero, it does not contribute to the change in total feedback parameter.

The results in Fig. 2 are thus consistent with the expected effect of a stability decrease following hypothesis 2: a decrease in low cloud amount (causing a more positive shortwave cloud feedback), and a less negative lapse rate feedback, these two effects jointly accounting for most of the increase in feedback parameter and climate sensitivity. While changes in factors other than stability – particularly local SST, subsidence, and free-tropospheric humidity – may also affect the evolution of the cloud response to global warming (29, 30), previous evidence from climate model experiments suggests that the stability effect dominates the cloud response to evolving tropical SST patterns (15). In further support for this conclusion, the relationship between tropospheric stability and feedbacks broadly holds across models: a larger stability decrease is associated with a larger increase in feedback parameter (Fig. S3, Text S1–S2). Stability changes account for less than half of the inter-model spread in net feedback changes, however ($r^2 = 0.40$, Fig. S3a), indicating that effects other than stability must also contribute to this spread (Text S2).

The joint effect of cloud and lapse rate feedbacks accounts for about 70% of the change in net feedback in our set of models, leaving part of the change unexplained. We have calculated how much of the evolution in global feedback parameter can be ascribed to a change in spatial weighting of local feedbacks as the warming pattern evolves, following hypothesis 1 (Fig. S4). The result suggests that the increases in surface albedo and relative humidity feedbacks are in part associated with the evolution of the warming pattern (0.05 and 0.04 W m^{-2} K^{-1} respectively; Text S3). While the increase in surface albedo feedback is consistent with the evolution towards enhanced high-latitude warming (Text S3; 7), the mechanisms of change in global relative humidity feedback (via either of the hypotheses or alternative mechanisms) remain unknown.

The linkage between climate feedbacks and tropospheric stability is particularly striking when considering the spatial distribution of the changes. Generally speaking, the feedbacks become more positive in regions where the EIS response decreases (compare Figs. 1b and 3), and vice-versa. The largest increase in feedback parameter occurs in the tropical Central and East Pacific, where the EIS response becomes substantially more negative as the planet warms. Although the EIS change over the Southern Ocean is comparable or larger in magnitude, the local change in cloud feedback is generally small; this may be because processes unrelated to tropospheric stability dominate the cloud response to warming at high southern latitudes. Comparing panels (c) and (d) in Fig. 3 confirms that the feedback decomposition accurately captures the actual evolution of changes in top-of-atmosphere net radiation, so that the spatial feedback patterns are not artifacts of the methodology.

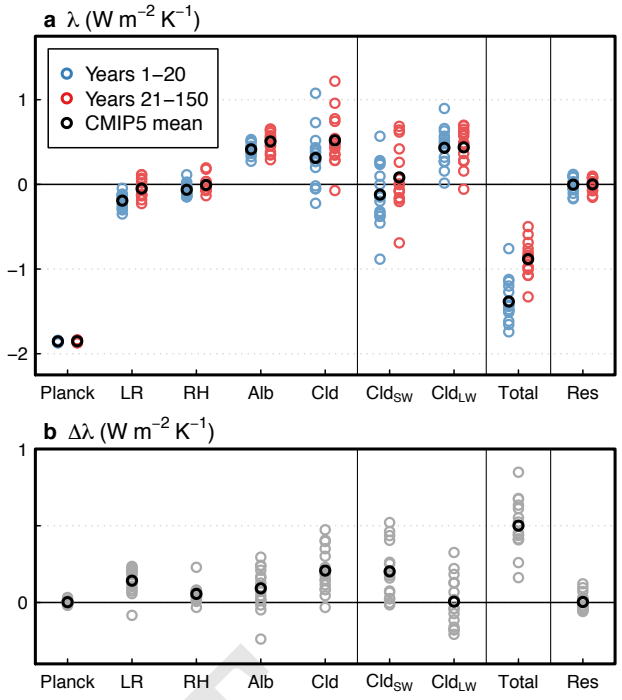

Fig. 2. Global-mean feedback parameter, calculated by the Gregory method (1), decomposed into contributions from uniform vertical warming (Planck feedback), non-uniform vertical warming (lapse rate), and changes in relative humidity, surface albedo, and clouds. The cloud term is further broken down into shortwave and longwave changes. "Total" refers to the sum of the feedbacks; the residual is the difference between the sum of the kernel-derived feedbacks and the actual feedback based on net top-of-atmosphere radiation (Materials and Methods). Shown are (a) the feedbacks calculated separately for the early (years 1–20) and late (21–150) periods, and (b) the difference taken as late minus early period. Blue, red and gray circles denote individual models (Table S1), while black circles are mean values.

Observed relationship between tropospheric stability and radiative budget. We have shown the existence of a relationship between SST pattern, tropospheric stability, and the radiative budget in climate models. Can a similar link be observed in the real world to confirm the realism of the modeled responses? Reliable satellite observations of the Earth's radiative budget are too short to allow for meaningful trend calculations. However, the proposed relationship between long-term changes in stability and radiative balance may also hold in the context of interannual variations. Climate models show qualitatively similar interannual relationships between SST, EIS and the radiative budget in the context of unforced variability to those found at decadal time scales under abrupt CO_2 quadrupling (compare Figs. 1, 3, and S5). In the following, we will demonstrate from observations that real-world year-to-year fluctuations in tropospheric stability are associated with SST and radiative anomalies consistent with the evolution of these variables in climate models.

Figure 4 shows the patterns of SST, EIS, cloud-radiative effect (CRE, defined as all-sky minus clear-sky net down-

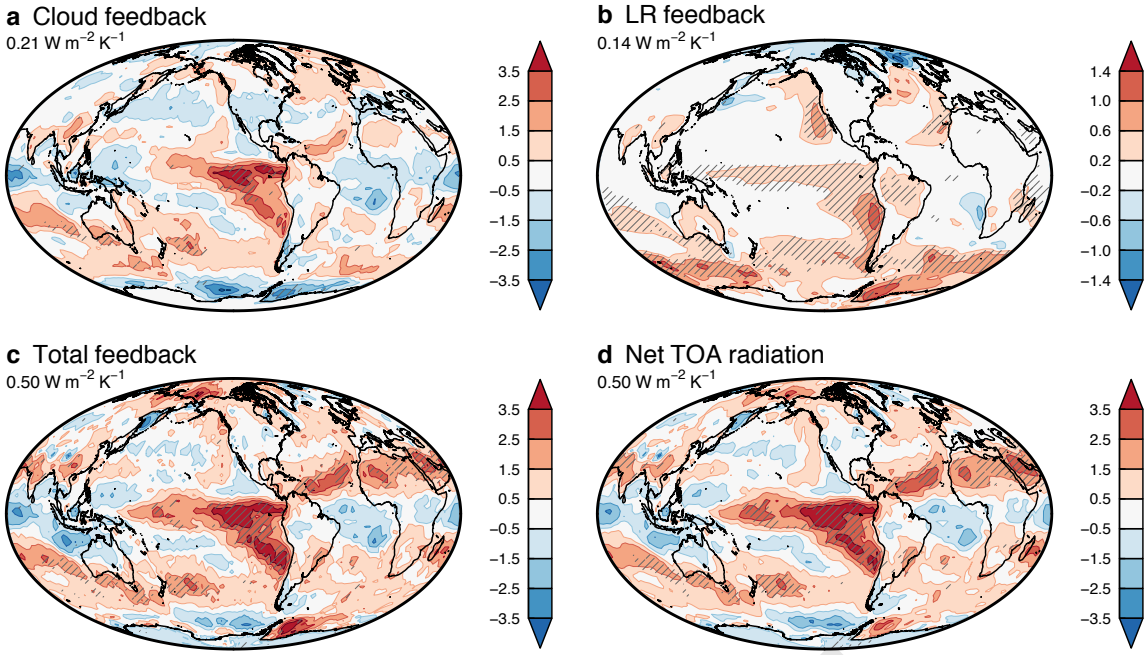

Fig. 3. Multi-model mean spatial patterns of changes in climate feedback, calculated as late (years 21–150) minus early (1–20) period. The total feedback in (c) is the sum of the kernel-derived feedbacks (Materials and Methods), while (d) shows the actual feedback based on the regression of net top-of-atmosphere radiation onto global-mean surface temperature. Numbers in the top left corner of each panel denote global-mean values. Hatching denotes a multi-model mean anomaly larger than one standard deviation.

ward top-of-atmosphere radiation), and net downward top-of-atmosphere radiation, all regressed onto annual- and global-mean EIS anomalies, using 16 years of gridded observational and reanalysis data (note that global-mean EIS excludes regions poleward of 50°; Materials and Methods). Since the regression coefficients would represent changes consistent with a 1-K global-mean EIS increase, we multiply the coefficients by the multi-model mean change in the derivative of EIS with respect to global-mean surface temperature (-0.16 K K^{-1}; Fig. 1b), to obtain observed anomalies comparable in sign and magnitude with the model ensemble. Note that the impact of any changes in global-mean surface temperature has been regressed out (Materials and Methods), to minimize the contribution of the Planck response to the global-mean radiative anomalies. The observed SST pattern associated with an EIS decrease features positive SST anomalies in the tropical and subtropical East Pacific (Fig. 4a). Although no substantial cooling is observed in the warm pool, the anomalous east–west SST gradient across the tropical Pacific is in broad qualitative agreement with the difference between patterns of SST change in climate models (Fig. 1a), causing a decrease in stability in the East Pacific (Fig. 4b).

Consistent with observed relationships between EIS and low cloud, the EIS decrease coincides with a region of positive CRE anomaly, which is reflected in the net top-of-atmosphere radiative change (Fig. 4c–d). The net observed global radiative anomaly (0.62 W m^{-2} K^{-1}) is larger than the multi-model-mean radiative response associated with a -0.16 K K^{-1} EIS change (0.50 W m^{-2} K^{-1}); however, considering the differences in observed SST and EIS patterns relative to the forced climate change signal in models (compare Fig. 1 with Fig. 4a–b), and given the relatively low signal-to-noise ratio in the short observational record of 16 years, the agreement between observations and models should be interpreted qualitatively, rather than quantitatively. In further support of our findings, similar relationships between tropical SST pattern and low cloud amount have been observed in the context of decadal trends over the 1983–2005 period (15).

CRE anomalies can be affected not only by changes in clouds, but also by non-cloud anomalies in temperature, moisture and surface albedo. By adjusting the CRE anomalies for non-cloud factors (Materials and Methods), we confirm the contribution of clouds to the stability-induced interannual radiative anomalies in observations and models (Figs. S6a, S7a). Decomposing the stability-induced radiative changes into individual components using kernels, we find that lapse rate changes also contribute to the positive radiative anomalies in the East Pacific and in the global mean (Figs. S6b, S7b), but note that the total kernel-derived radiative changes overestimate the actual observed radiative anomalies by about 13% (Fig. S6c–d). Differences between kernel-derived and observed anomalies could be associated with errors in reanalysis temperature and moisture data, inaccuracies in the radiative kernel method (31, 32), or errors in satellite radiances (33). Despite these limitations, our observational analysis does qualitatively support the notion that decreasing tropospheric stability promotes a decrease in radiative cooling to space through changes in clouds and tropospheric lapse rate, consistent with the evolution towards higher effective climate sensitivity in CO_2-forced climate model experiments.

Summary and Discussion

Climate models predict that, as the planet warms, the response of tropospheric stability to global warming will gradually be-

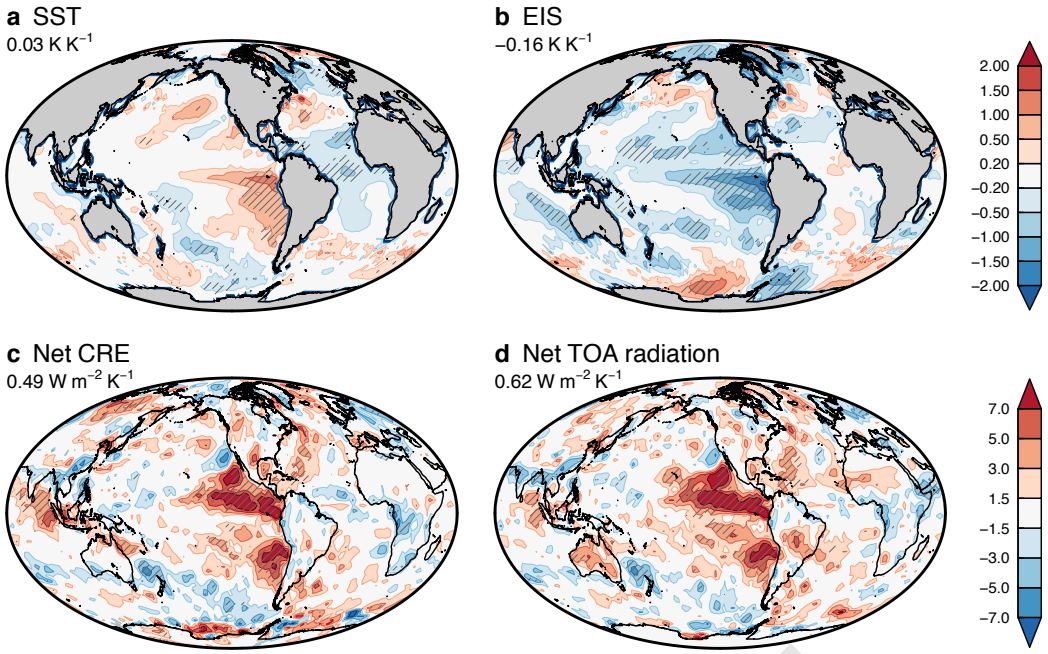

Fig. 4. Anomalies of (a) SST, (b) EIS, (c) net CRE, and (d) net top-of-atmosphere radiation regressed onto global- and annual-mean EIS anomalies, for the period December 2000–November 2016 based on global gridded observational and reanalysis datasets (Materials and Methods). The regression coefficients are rescaled by a factor of -0.16 K K^{-1} EIS change, to aid comparison with the results in Figs. 1 and 3. Numbers in the top left corner of each panel denote global-mean values. Hatching indicates a statistically significant regression coefficient at the 5% level.

come more negative, in a manner determined by the evolution of SSTs. The change in stability favors a decrease in low cloud cover (a positive shortwave cloud feedback) and a less negative lapse rate feedback. Although these effects dominate, part of the increase in net feedback (mainly due to changes in surface albedo and humidity) cannot be simply explained by the change in stability; these additional contributions result either from a change in the spatial weighting of local feedbacks (7), or from other unexplained mechanisms. The evolution of climate feedbacks exhibits a spatial structure that closely matches the distribution of stability changes, being most pronounced in the tropical East Pacific, a region characterized by relatively low SST, stable conditions, and extensive marine low cloud. We further show that qualitatively similar relationships between SST pattern, tropospheric stability, and the radiative budget are found in observations on interannual time scales. Therefore, to the extent that future patterns of SST change resemble those of past variability, observational evidence is consistent with the evolution towards a higher effective climate sensitivity during the transient response to CO_2 forcing in climate models.

Further work is needed to fully understand the implications of SST anomaly patterns for tropospheric stability and the Earth's radiative budget. In particular, the relative importance of anomalous zonal SST gradients within the tropics versus anomalous meridional gradients between tropics and extratropics remains unknown. While our results suggest a crucial role for zonal gradients within the tropical Pacific, previous work has suggested that anomalous meridional SST gradients (or relatedly, anomalies in the meridional gradient of ocean heat uptake) could have large impacts on climate feedbacks (18–20). Further model experiments with idealized (18, 19) and realistic (14, 15, 19, 34) SST anomaly patterns will provide additional insight into the relationships between global anomalies in SST, stability, and the radiative budget.

Materials and Methods

Model data. The evolution of SST, EIS, and climate feedbacks is analyzed in Coupled Model Intercomparison Project phase 5 (CMIP5) climate model output during the 150 years following abrupt quadrupling of atmospheric CO_2 concentrations starting from pre-industrial conditions (the "abrupt4xCO2" experiment). We analyze monthly-mean values of temperature, specific humidity, surface albedo, and upward and downward radiative fluxes at the top of atmosphere (TOA) for both all- and clear-sky conditions. The 25 models with available data are listed in Table S1. To remove any potential model drift, anomalies are calculated by subtracting the pre-industrial (piControl) integration from the corresponding parallel abrupt4xCO2 integration. Only the first ensemble member is used for each model.

Feedback analysis. The contributions of temperature, moisture, surface albedo, and clouds to changes in TOA radiation are diagnosed separately for each month of the abrupt4xCO2 integration using radiative kernels (31, 32). Kernels are partial derivatives of the TOA radiative flux relative to temperature, water vapor mixing ratio, and surface albedo at each model grid point. Multiplying the kernels by the changes in each of these variables provides an estimate of their contributions to TOA flux changes. Water vapor changes are partitioned into changes consistent with constant relative humidity (included in the temperature feedbacks), and changes in relative humidity (35). The kernels are also used to adjust cloud-radiative effect (CRE) anomalies for changes in non-cloud effects to obtain an estimate of the radiative changes due to clouds only (31). In this study we use kernels calculated with the Community Atmospheric Model version 5 (36).

The kernel-derived contributions to TOA flux anomalies are aggregated into annual-mean values for each model, and converted to feedbacks by regressing the radiative flux time series onto global-mean surface air temperature (1, 37). Ordinary least-squares regressions are calculated separately for years 1–20 and 21–150 of the abrupt4xCO2 experiment (9). We verify the accuracy of the kernel-derived feedbacks by a clear-sky linearity test (32, 37), whereby we compare the kernel-based sum of clear-sky TOA feedbacks with the actual clear-sky feedback obtained by regressing clear-sky net TOA radiation onto global-mean surface temperature. In our results we only include the 15 models for which the error in kernel-based clear-sky feedback is less than 15% of the actual value in both regression periods (bolded model names in Table S1; 37). (Since CRE anomalies are based on model output, testing the kernel decomposition with clear-sky feedbacks ensures that only kernel-derived quantities are used in the test (32).) The results of the feedback analysis remain qualitatively unchanged if we include models with clear-sky errors larger than 15% in the calculations (Table S1), or if we use an alternative set of radiative kernels (31). The feedback residuals are computed as actual minus sum of kernel-derived feedbacks (where the actual feedback is the regression slope of net TOA radiation against global-mean temperature). ECS values (Fig. S2b) are calculated as the x-intercepts of the least-squares fits over years 1–20 and 21–150.

Effect of EIS variations. The impact of year-to-year variations in tropospheric stability on the radiative budget is assessed by regression analysis in observations and pre-industrial model integrations (using 50 years of data for each model). As a simple measure of large-scale stability changes, we use global-mean EIS, but excluding grid points poleward of 50°; including those grid points tends to emphasize high-latitude changes at the sea ice margins in climate models, likely related to sea ice variability. Since global-mean surface temperature anomalies associated with EIS variability will not generally be zero, a component of the associated radiative changes will be due to a Planck response that is not a direct result of the stability-driven cloud and lapse rate responses. Therefore, the fields are jointly regressed onto annual global-mean temperature and EIS anomalies to isolate the EIS effect, and we present results for the regression slopes associated with EIS only.

Observations. We use Clouds and the Earth's Radiant Energy System (CERES) monthly gridded global satellite observations of all- and clear-sky TOA radiative fluxes during December 2000 – November 2016. Prior to analysis the values are detrended at each grid point by removing a linear trend estimated by least-squares regression. To estimate the relationship between SST, EIS, and the observed radiative budget, we use ERA-Interim (38) reanalysis fields of surface and atmospheric temperature, with which we compute annual detrended SST and EIS anomalies. In addition to reanalysis temperature, we also use moisture and surface albedo reanalysis values in combination with radiative kernels to decompose the TOA radiative flux anomalies, and to adjust the CRE anomalies for non-cloud effects.

ACKNOWLEDGMENTS. We thank Steve Klein, an anonymous reviewer, and the Editor for helpful comments. PC was supported by the European Research Council grant "ACRCC" (grant number 339390); JMG was supported by the NCAS-Climate program.

1. Gregory JM, et al. (2004) A new method for diagnosing radiative forcing and climate sensitivity. *Geophysical Research Letters* 31(3):L03205.
2. Murphy JM (1995) Transient Response of the Hadley Centre Coupled Ocean-Atmosphere Model to Increasing Carbon Dioxide. Part I: Control Climate and Flux Adjustment. *Journal of Climate* 8(1):36–56.
3. Williams KD, Ingram WJ, Gregory JM (2008) Time Variation of Effective Climate Sensitivity in GCMs. *Journal of Climate* 21(19):5076–5090.
4. Senior CA, Mitchell JFB (2000) The time-dependence of climate sensitivity. *Geophysical Research Letters* 27(17):2685–2688.
5. Winton M, Takahashi K, Held IM (2010) Importance of Ocean Heat Uptake Efficacy to Transient Climate Change. *Journal of Climate* 23(9):2333–2344.
6. Andrews T, Gregory JM, Webb MJ, Taylor KE (2012) Forcing, feedbacks and climate sensitivity in CMIP5 coupled atmosphere-ocean climate models. *Geophysical Research Letters* 39(9):L09712.
7. Armour KC, Bitz CM, Roe GH (2013) Time-Varying Climate Sensitivity from Regional Feedbacks. *Journal of Climate* 26(13):4518–4534.
8. Meraner K, Mauritsen T, Voigt A (2013) Robust increase in equilibrium climate sensitivity under global warming. *Geophysical Research Letters* 40(22):5944–5948.
9. Andrews T, Gregory JM, Webb MJ (2015) The Dependence of Radiative Forcing and Feedback on Evolving Patterns of Surface Temperature Change in Climate Models. *Journal of Climate* 28(4):1630–1648.
10. Paynter D, Frölicher TL (2015) Sensitivity of radiative forcing, ocean heat uptake, and climate feedback to changes in anthropogenic greenhouse gases and aerosols. *Journal of Geophysical Research: Atmospheres* 120(19):9837–9854.
11. Knutti R, Rugenstein MAA (2015) Feedbacks, climate sensitivity and the limits of linear models. *Philosophical transactions. Series A, Mathematical, physical, and engineering sciences* 373(2054):20150146.
12. Armour KC (2017) Energy budget constraints on climate sensitivity in light of inconstant climate feedbacks. *Nature Climate Change*.
13. Proistosescu C, Huybers PJ (2017) Slow climate mode reconciles historical and model-based estimates of climate sensitivity. *Science Advances* 3(7).
14. Gregory JM, Andrews T (2016) Variation in climate sensitivity and feedback parameters during the historical period. *Geophysical Research Letters* 43(8):3911–3920.
15. Zhou C, Zelinka MD, Klein SA (2016) Impact of decadal cloud variations on the Earth's energy budget. *Nature Geoscience* 9(12):871–874.
16. Zhou C, Zelinka MD, Klein SA (2017) Analyzing the dependence of global cloud feedback on the spatial pattern of sea surface temperature change with a Green's function approach. *Journal of Advances in Modeling Earth Systems*.
17. Andrews T, Webb MJ (2017) The dependence of global cloud and lapse-rate feedbacks on the spatial structure of tropical Pacific warming. *Journal of Climate* pp. JCLI–D–17–0087.1.
18. Rose BEJ, Armour KC, Battisti DS, Feldl N, Koll DDB (2014) The dependence of transient climate sensitivity and radiative feedbacks on the spatial pattern of ocean heat uptake. *Geophysical Research Letters* 41(3):1071–1078.
19. Rugenstein MAA, Caldeira K, Knutti R (2016) Dependence of global radiative feedbacks on evolving patterns of surface heat fluxes. *Geophysical Research Letters* 43(18):9877–9885.
20. Haugstad AD, Armour KC, Battisti DS, Rose BEJ (2017) Relative roles of surface temperature and climate forcing patterns in the inconstancy of radiative feedbacks. *Geophysical Research Letters* 44.
21. Held IM, et al. (2010) Probing the Fast and Slow Components of Global Warming by Returning Abruptly to Preindustrial Forcing. *Journal of Climate* 23(9):2418–2427.
22. Xie SP, et al. (2010) Global Warming Pattern Formation: Sea Surface Temperature and Rainfall. *Journal of Climate* 23(4):966–986.
23. Armour KC, Marshall J, Scott JR, Donohoe A, Newsom ER (2016) Southern Ocean warming delayed by circumpolar upwelling and equatorward transport. *Nature Geoscience* 9(7):549–554.
24. Long SM, Xie SP, Zheng XT, Liu Q (2014) Fast and Slow Responses to Global Warming: Sea Surface Temperature and Precipitation Patterns. *Journal of Climate* 27(1):285–299.
25. Wood R, Bretherton CS (2006) On the Relationship between Stratiform Low Cloud Cover and Lower-Tropospheric Stability. *Journal of Climate* 19(24):6425–6432.
26. Sobel AH, Held IM, Bretherton CS (2002) The ENSO Signal in Tropical Tropospheric Temperature. *Journal of Climate* 15(18):2702–2706.
27. Flannaghan TJ, et al. (2014) Tropical temperature trends in Atmospheric General Circulation Model simulations and the impact of uncertainties in observed SSTs. *Journal of Geophysical Research: Atmospheres* 119(23):13,327–13,337.
28. Qu X, Hall A, Klein SA, Caldwell PM (2015) The strength of the tropical inversion and its response to climate change in 18 CMIP5 models. *Climate Dynamics* 45(1-2):375–396.
29. Qu X, Hall A, Klein SA, DeAngelis AM (2015) Positive tropical marine low-cloud cover feedback inferred from cloud-controlling factors. *Geophysical Research Letters* 42(18):7767–7775.
30. Myers TA, Norris JR (2016) Reducing the uncertainty in subtropical cloud feedback. *Geophysical Research Letters* 43(5):2144–2148.
31. Soden BJ, et al. (2008) Quantifying Climate Feedbacks Using Radiative Kernels. *Journal of Climate* 21(14):3504–3520.
32. Shell KM, Kiehl JT, Shields CA (2008) Using the Radiative Kernel Technique to Calculate Climate Feedbacks in NCAR's Community Atmospheric Model. *Journal of Climate* 21(10):2269–2282.
33. Loeb NG, et al. (2009) Toward Optimal Closure of the Earth's Top-of-Atmosphere Radiation Budget. *Journal of Climate* 22(3):748–766.
34. Webb MJ, et al. (2017) The Cloud Feedback Model Intercomparison Project (CFMIP) contribution to CMIP6. *Geoscientific Model Development* 10(1):359–384.
35. Held IM, Shell KM (2012) Using Relative Humidity as a State Variable in Climate Feedback Analysis. *Journal of Climate* 25(8):2578–2582.
36. Pendergrass AG, Conley A, Vitt F (2017) Surface and top-of-atmosphere radiative feedback kernels for CESM-CAM5. *Earth System Science Data Discussions* pp. 1–14.
37. Caldwell PM, Zelinka MD, Taylor KE, Marvel K (2016) Quantifying the Sources of Intermodel Spread in Equilibrium Climate Sensitivity. *Journal of Climate* 29(2):513–524.
38. Dee DP, et al. (2011) The ERA-Interim reanalysis: configuration and performance of the data assimilation system. *Quarterly Journal of the Royal Meteorological Society* 137(656):553–597.
39. Gordon ND, Klein SA (2014) Low-cloud optical depth feedback in climate models. *Journal of Geophysical Research: Atmospheres* 119(10):6052–6065.

Supporting information for "Relationship of tropospheric stability to climate sensitivity and Earth's observed radiation budget"

Ceppi et al. 10.1073/pnas.XXXXXXXXXX

Supporting Information (SI)

Text S1: Change in global feedback versus change in global EIS response. In our calculation of the relationships between the changes in cloud feedback and the changes in global EIS response per unit warming, one model, MIROC-ESM, clearly stands out as an outlier (red circles in Fig. S3). This model features both the most positive change in EIS response, and the most positive change in shortwave and net cloud feedback. In a previous analysis of the relationships between shortwave cloud-radiative effect and meteorology in tropical subsidence regions, MIROC-ESM was the only CMIP5 model to simulate a substantial *positive* relationship between shortwave cloud-radiative effect and EIS (30, their Figs. 2b and S1), consistent with Fig. S3d and contrary to observational evidence.

We have therefore excluded MIROC-ESM from the calculation of the slopes and correlation coefficients in Fig. S3. Including MIROC-ESM would result in a much weaker correlation coefficient between change in cloud feedback and change in EIS response ($r = [-0.34, -0.18]$ for the shortwave and net components, respectively).

Finally, note that the *positive* relationship between longwave cloud feedback changes and changes in EIS response (Fig. S3e) is not inconsistent with our reasoning, considering that shortwave and longwave cloud feedbacks are generally anticorrelated. The shortwave impact of stability changes dominates the spread in net cloud feedback (Fig. S3f), consistent with our understanding that the inter-model spread in cloud feedbacks is mainly associated with low clouds.

Text S2: Inter-model spread in climate feedback changes. The relationships in Fig. S3 suggest that inter-model differences in the evolution of tropospheric stability (as quantified by EIS) contribute to differences in the evolution of the climate feedbacks. However, the substantial scatter in Fig. S3 indicates that global-mean stability changes cannot fully account for the inter-model spread in feedback changes. Here, we briefly discuss other possible contributions to the spread in feedback changes.

First, the sensitivity of climate feedbacks to stability changes is expected to vary from model to model. This applies particularly to cloud feedbacks, since the sensitivity of low clouds to stability changes varies considerably among CMIP5 models (e.g., 30, their Fig. 1). Hence, even if the cloud feedback changes were driven entirely by changes in tropospheric stability in all climate models, we would not obtain a perfect linear relationship in Fig. S3.

Second, processes unrelated to stability must contribute to the evolution of climate feedbacks. For example, the spread in albedo feedback changes is large in our set of models (Fig. 2b) and it is unrelated to the global-mean EIS change index used in Fig. S3 ($r = -0.02$). The evolution of albedo feedbacks is likely related to the evolution of the local SST response per degree global warming in different models, as suggested by Fig. S4. Cloud responses are controlled by a variety of environmental factors other than stability (e.g., 29). Furthermore, as discussed in the main text, the mechanisms of the evolution of the relative humidity feedback remain unknown; the spread in relative humidity feedback change is only marginally related to the EIS index considered here ($r = -0.27$).

Text S3: Climate feedbacks based on the local feedback perspective. One hypothesis for the evolution of the feedback parameter is based on the idea that the spatial pattern of warming determines the relative contributions of local feedbacks to the global-mean radiative budget; consequently, a change in the spatial warming pattern will cause a change in the global feedback parameter if the local feedbacks vary in space (7). In this perspective, the increasing global-mean feedback in global warming simulations as time passes results from the evolution of the surface warming pattern towards enhanced warming in regions of relatively positive local feedbacks. In this section, we demonstrate that this perspective cannot adequately explain the time evolution of the global feedback parameter seen in CMIP5 experiments.

In the local feedback perspective, climate feedbacks are assumed to be constant in time, but spatially varying (i.e. they depend on geographical location x). The effective global-mean feedback λ_{eff} can then be understood as a spatial average of local feedbacks $\lambda(x)$ weighted by the local contributions to global-mean warming:

$$\lambda_{\text{eff}}(t) = \overline{\lambda(x)P(x,t)}, \qquad [1]$$

where $P(x,t)$ is the normalized warming pattern (defined as local surface warming per unit global warming) and overbars denote spatial averages. Under the assumption of time-independent local feedbacks, any temporal variations in the effective global-mean feedback parameter must arise from variations in $P(x,t)$.

We first derive the local feedbacks $\lambda(x)$. Since they are assumed constant, we may calculate them using any part of the experiment; we compute them by taking the mean of the last 20 years of the abrupt4xCO2 integrations, minus the mean of the first 10 years. This ensures that rapid adjustments are excluded from the calculation, while maximizing the warming-induced signal. We divide the time-mean kernel-derived radiative anomalies at each point (for each of the components shown in Fig. S4) by the time-mean local surface temperature anomaly. This procedure yields better results than regressing the local radiative anomalies against local warming, because the low signal-to-noise ratio in local radiative anomalies means that the regression slopes are noisy and not robust. Note that for some models, the surface temperature response may be near zero in some regions, resulting in large, unphysical local feedback values when dividing the radiative anomalies by the

temperature anomalies. However, we have verified that these unphysical values have relatively little impact on the global-mean feedback values, and similar results are obtained if these grid points are excluded from our calculations.

Effective global-mean feedbacks are then calculated for years 1–20 and 21–150 following Eq. 1. The warming patterns $P(x,t)$ are calculated by regressing local surface air temperature onto global-mean surface air temperature over each of the two periods. As shown in Fig. S4, the total effective global feedback derived assuming constant local feedbacks only weakly increases in time (0.05 W m^{-2} K^{-1} in the multi-model mean). This means that a change in spatial weighting of constant local feedbacks can only play a secondary role for the evolution of the relationship between global-mean radiative imbalance and global-mean temperature; this evolution must result primarily from changes in the local feedbacks, rather than from changes in the spatial pattern of warming.

The results do suggest, however, that a linear dependence of feedback processes on local temperature may partly explain the evolution of the surface albedo feedback (0.05 W m^{-2} K^{-1}). This is unsurprising, since the warming pattern evolves towards enhanced high-latitude warming over time (Fig. 1; 7). We have not investigated the mechanism for the weak increase in relative humidity feedback obtained assuming constant local feedbacks (0.04 W m^{-2} K^{-1}). We also note that changes in the spatial weighting of local feedbacks may account for a substantial fraction of the increase in global feedbacks in a few of the models (Fig. S4b).

Note that even though Fig. S4 indicates that the hypothesis of constant local feedbacks cannot capture the increase in global cloud feedback over time, it may still explain the evolution of cloud feedback in some regions, where the cloud feedback processes are mainly controlled by local temperature rather than by remote factors – for example phase change feedbacks in high-latitude regions (39).

Table S1. List of Coupled Model Intercomparison Project phase 5 (CMIP5) climate models with their feedback values (in W m^{-2} K^{-1}) calculated over years 1–20 and (in parentheses) years 21–150. The 15 models listed in bold typeface were used in the analysis (Materials and Methods). The residual represents the difference between the actual feedback (calculated by regressing net top-of-atmosphere radiative anomalies against global-mean temperature) and the sum of radiative kernel-derived feedbacks (Materials and Methods).

Model name	Planck	Lapse rate	RH	Albedo	Cloud	LW cloud	SW cloud	Total	Residual
ACCESS1.0	-1.84 (-1.85)	-0.26 (-0.01)	-0.01 (-0.01)	0.37 (0.59)	0.41 (0.48)	0.63 (0.31)	-0.22 (0.17)	-1.33 (-0.80)	0.25 (0.23)
ACCESS1.3	-1.85 (-1.85)	-0.18 (-0.03)	-0.10 (-0.02)	0.50 (0.54)	0.37 (0.78)	0.27 (0.16)	0.10 (0.62)	-1.27 (-0.59)	0.10 (0.10)
BCC-CSM1.1	-1.87 (-1.87)	-0.12 (0.11)	-0.07 (-0.06)	0.41 (0.64)	0.20 (0.28)	0.54 (0.36)	-0.34 (-0.08)	-1.44 (-0.89)	0.09 (0.03)
BCC-CSM1.1(m)	-1.86 (-1.87)	-0.14 (0.06)	-0.12 (-0.07)	0.45 (0.55)	0.27 (0.45)	0.27 (0.45)	-0.00 (-0.00)	-1.40 (-0.88)	0.03 (0.01)
BNU-ESM	-1.87 (-1.85)	-0.04 (0.03)	0.01 (0.07)	0.64 (0.65)	0.17 (-0.08)	0.47 (0.36)	-0.31 (-0.44)	-1.08 (-1.19)	0.12 (0.06)
CanESM2	-1.86 (-1.85)	-0.22 (-0.07)	0.03 (-0.00)	0.38 (0.46)	0.52 (0.49)	0.90 (0.69)	-0.38 (-0.20)	-1.15 (-0.98)	-0.05 (0.08)
CCSM4	-1.85 (-1.87)	-0.12 (0.12)	-0.04 (-0.01)	0.51 (0.64)	-0.02 (0.28)	0.44 (0.28)	-0.46 (0.01)	-1.51 (-0.84)	-0.05 (-0.07)
CNRM-CM5	-1.86 (-1.85)	0.00 (-0.12)	-0.01 (-0.10)	0.67 (0.42)	0.13 (0.17)	0.40 (0.27)	-0.27 (-0.09)	-1.08 (-1.47)	0.03 (0.24)
FGOALS-s2	-1.87 (-1.87)	-0.10 (-0.06)	0.06 (0.06)	0.50 (0.69)	0.02 (0.03)	0.34 (0.53)	-0.32 (-0.50)	-1.39 (-1.15)	0.48 (0.41)
GFDL-CM3	-1.84 (-1.85)	-0.30 (-0.12)	-0.15 (-0.13)	0.44 (0.45)	0.73 (0.96)	0.45 (0.27)	0.28 (0.69)	-1.12 (-0.69)	-0.01 (0.09)
GFDL-ESM2G	-1.84 (-1.84)	-0.34 (-0.07)	0.08 (0.02)	0.25 (0.47)	-0.09 (0.60)	0.92 (0.34)	-1.01 (0.26)	-1.93 (-0.83)	0.36 (0.10)
GFDL-ESM2M	-1.83 (-1.83)	-0.33 (-0.12)	0.01 (0.02)	0.38 (0.40)	0.07 (0.28)	0.88 (0.26)	-0.80 (0.03)	-1.70 (-1.25)	0.34 (0.12)
GISS-E2-H	-1.85 (-1.85)	-0.18 (0.02)	0.11 (0.19)	0.40 (0.38)	-0.22 (-0.07)	0.66 (0.62)	-0.88 (-0.69)	-1.74 (-1.33)	-0.16 (-0.14)
GISS-E2-R	-1.84 (-1.86)	-0.35 (0.04)	0.15 (0.26)	0.32 (0.33)	-0.43 (0.05)	0.80 (0.63)	-1.23 (-0.58)	-2.14 (-1.19)	-0.24 (-0.14)
HadGEM2-ES	-1.85 (-1.85)	-0.14 (-0.04)	-0.00 (0.03)	0.47 (0.52)	0.34 (0.81)	0.59 (0.41)	-0.24 (0.40)	-1.18 (-0.52)	0.37 (0.18)
INMCM4	-1.87 (-1.84)	-0.05 (-0.13)	-0.05 (0.18)	0.53 (0.29)	-0.05 (0.42)	0.27 (0.49)	-0.32 (-0.07)	-1.49 (-1.07)	-0.17 (-0.15)
IPSL-CM5A-LR	-1.84 (-1.84)	-0.28 (-0.23)	-0.04 (0.00)	0.33 (0.35)	1.08 (1.22)	0.51 (0.58)	0.57 (0.64)	-0.76 (-0.50)	-0.11 (-0.08)
IPSL-CM5B-LR	-1.85 (-1.85)	-0.12 (-0.04)	-0.03 (0.03)	0.40 (0.36)	0.39 (0.74)	0.16 (0.48)	0.24 (0.26)	-1.20 (-0.76)	-0.00 (-0.03)
MIROC-ESM	-1.85 (-1.84)	-0.20 (-0.31)	-0.05 (-0.15)	0.71 (0.40)	0.28 (1.19)	0.65 (0.24)	-0.37 (0.96)	-1.10 (-0.70)	0.04 (0.06)
MIROC5	-1.86 (-1.83)	-0.21 (-0.17)	-0.07 (-0.00)	0.47 (0.59)	-0.08 (0.08)	0.26 (0.48)	-0.34 (-0.40)	-1.76 (-1.34)	0.03 (0.14)
MPI-ESM-LR	-1.85 (-1.84)	-0.27 (-0.18)	-0.15 (-0.07)	0.41 (0.58)	0.43 (0.54)	0.57 (0.70)	-0.14 (-0.16)	-1.43 (-0.98)	0.10 (0.07)
MPI-ESM-MR	-1.85 (-1.85)	-0.24 (-0.12)	-0.14 (-0.06)	0.41 (0.65)	0.33 (0.53)	0.48 (0.61)	-0.15 (-0.08)	-1.49 (-0.85)	0.09 (0.03)
MPI-ESM-P	-1.85 (-1.85)	-0.35 (-0.14)	-0.12 (-0.07)	0.27 (0.57)	0.43 (0.48)	0.63 (0.65)	-0.20 (-0.17)	-1.62 (-1.00)	0.12 (0.08)
MRI-CGCM3	-1.86 (-1.84)	-0.17 (-0.06)	-0.10 (-0.06)	0.37 (0.52)	0.28 (0.36)	0.02 (-0.06)	0.26 (0.42)	-1.48 (-1.07)	-0.06 (0.01)
NorESM1-M	-1.86 (-1.87)	-0.14 (0.07)	-0.00 (0.03)	0.40 (0.61)	-0.05 (0.35)	0.32 (0.28)	-0.37 (0.06)	-1.66 (-0.81)	0.02 (-0.02)
Mean (15 models)	-1.85 (-1.85)	-0.19 (-0.05)	-0.06 (-0.01)	0.41 (0.51)	0.31 (0.52)	0.43 (0.44)	-0.12 (0.08)	-1.38 (-0.88)	-0.00 (0.00)
Mean (all models)	-1.85 (-1.85)	-0.19 (-0.06)	-0.03 (0.00)	0.44 (0.51)	0.22 (0.46)	0.50 (0.41)	-0.28 (0.04)	-1.42 (-0.95)	0.07 (0.06)

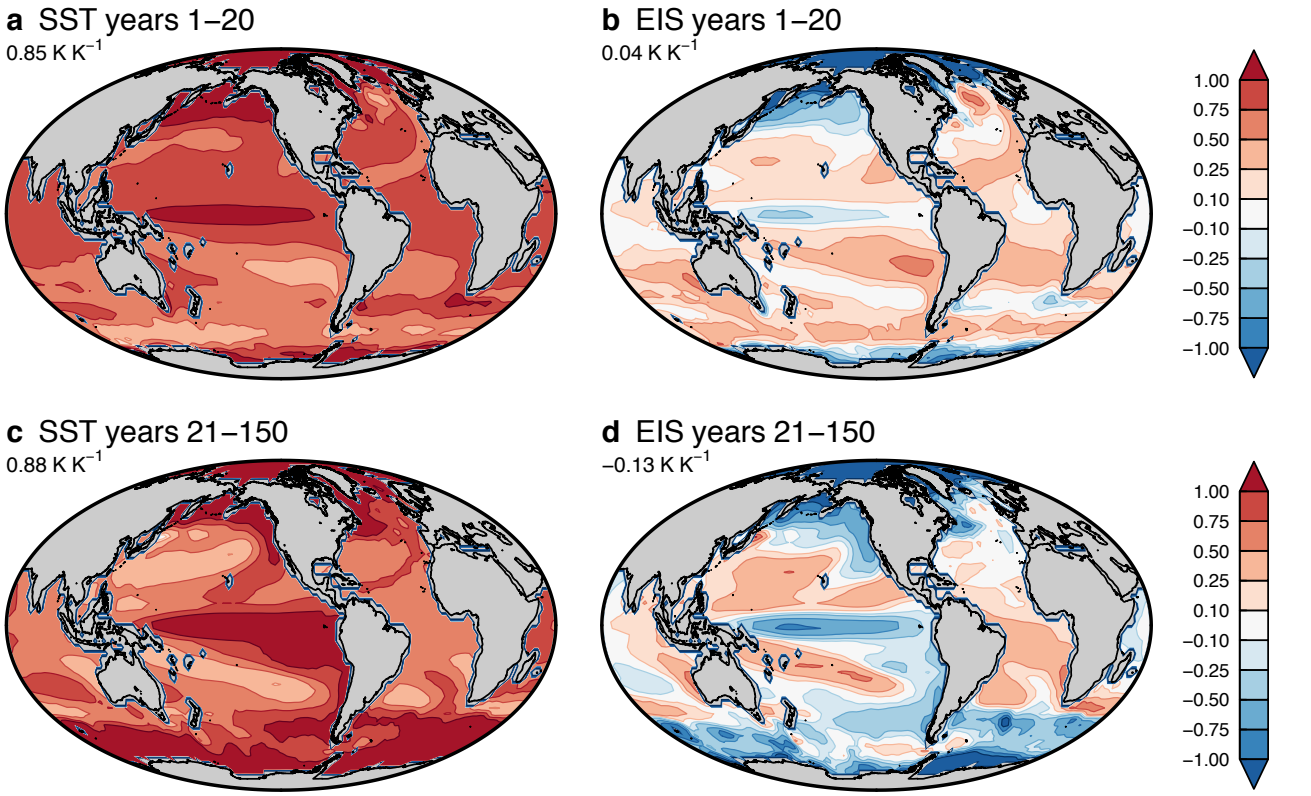

Fig. S1. Multi-model mean normalized changes in SST and EIS during years 1–20 (a,b) and 21–150 (c,d), calculated by regressing annual-mean SST and EIS against global-mean temperature during the respective periods. Numbers in the top left corner of each panel denote global-mean values.

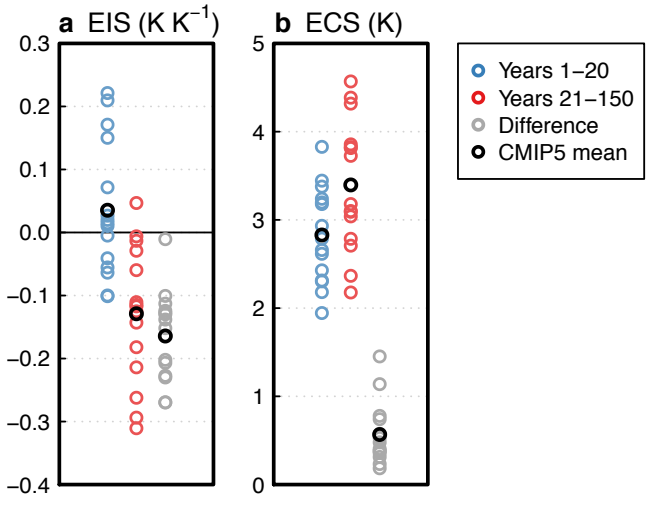

Fig. S2. Changes in annual-mean global-mean EIS (a) and ECS (b) during years 1–20 (blue), years 21–150 (red), and the difference between the two periods (gray). Each colored circle represents a model, and black circles denote multi-model means. EIS changes are calculated by regressing global-mean EIS onto global-mean temperature during each period. See the Materials and Methods section for the ECS calculation.

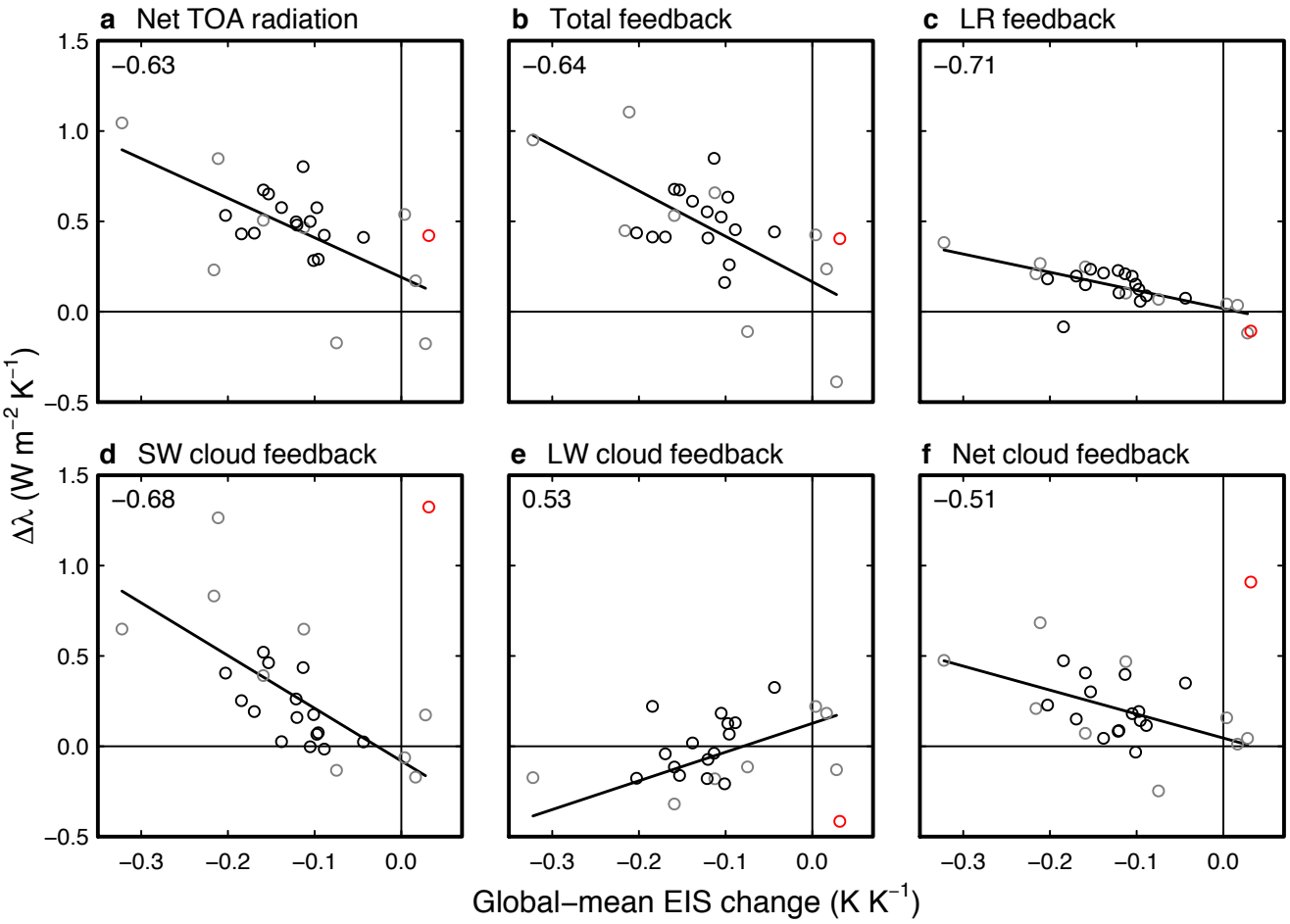

Fig. S3. Change in feedback parameter versus change in global-mean EIS response per unit warming. Shown are changes in (a) net feedback based on TOA radiation, (b) the sum of kernel-derived feedbacks, (c) lapse rate feedback, (d)–(f) shortwave, longwave, and net cloud feedback. The changes are calculated as late (years 21–150) minus early (1–20) period. Black lines denote ordinary least-squares regression slopes. Black circles denote the 15 models used in the analysis; the red circle represents an outlier model, MIROC-ESM, excluded from the calculation of the regression slopes and correlation coefficients (Text S1); and gray circles represent the remaining 9 models (Table S1). The correlation coefficients are calculated for all models, minus MIROC-ESM. Note that regions poleward of 50° are excluded from the global-mean EIS calculation (Materials and Methods).

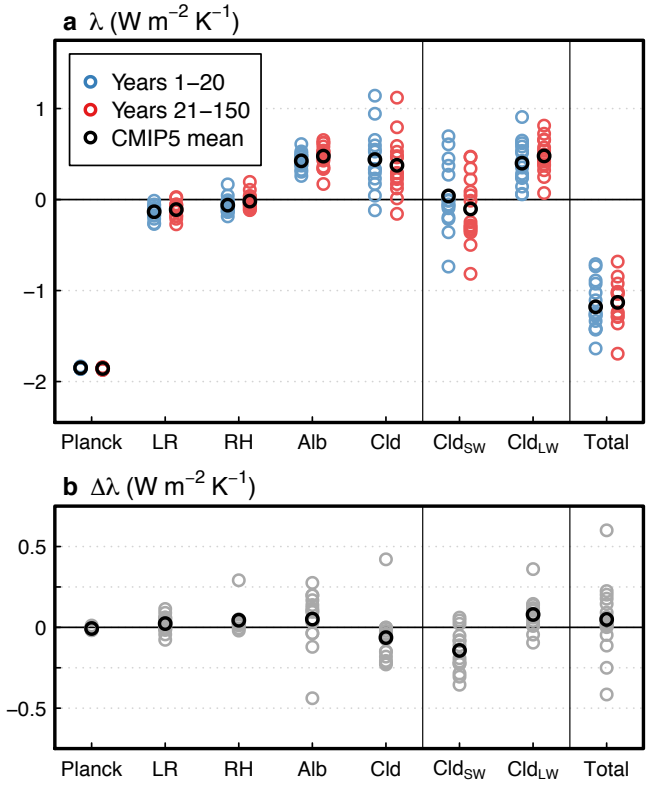

Fig. S4. As in Fig. 2 but showing feedback values calculated following the local feedback perspective of Armour et al. (7). See Text S3 for details of the calculation method.

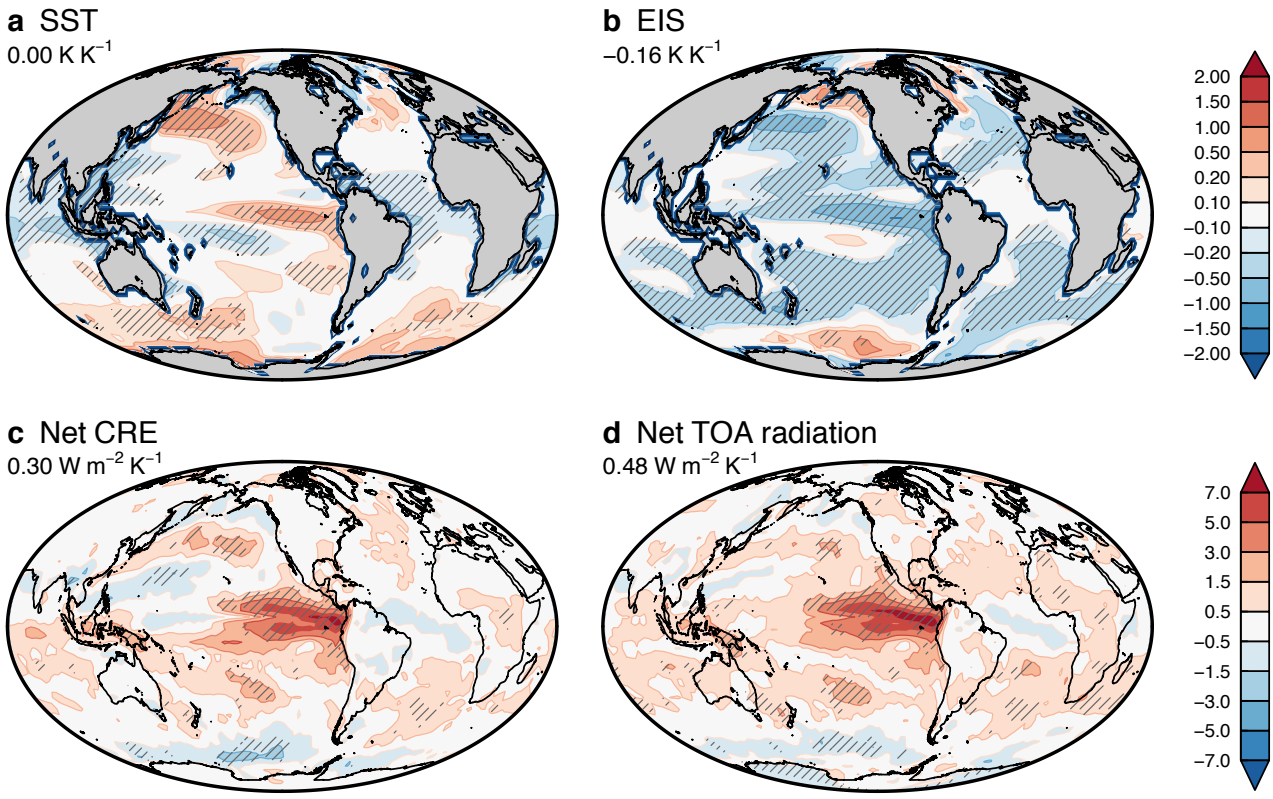

Fig. S5. As in Fig. 4, but using pre-industrial control data in the 15 models used in the analysis. Shown are the multi-model mean regression patterns, rescaled to yield anomalies consistent with a -0.16 K K^{-1} global-mean EIS change to aid comparison with Figs. 1 and 3. Hatching denotes a multi-model mean anomaly larger than one standard deviation. Note that the effect of changes in global-mean surface temperature has been regressed out (Materials and Methods).

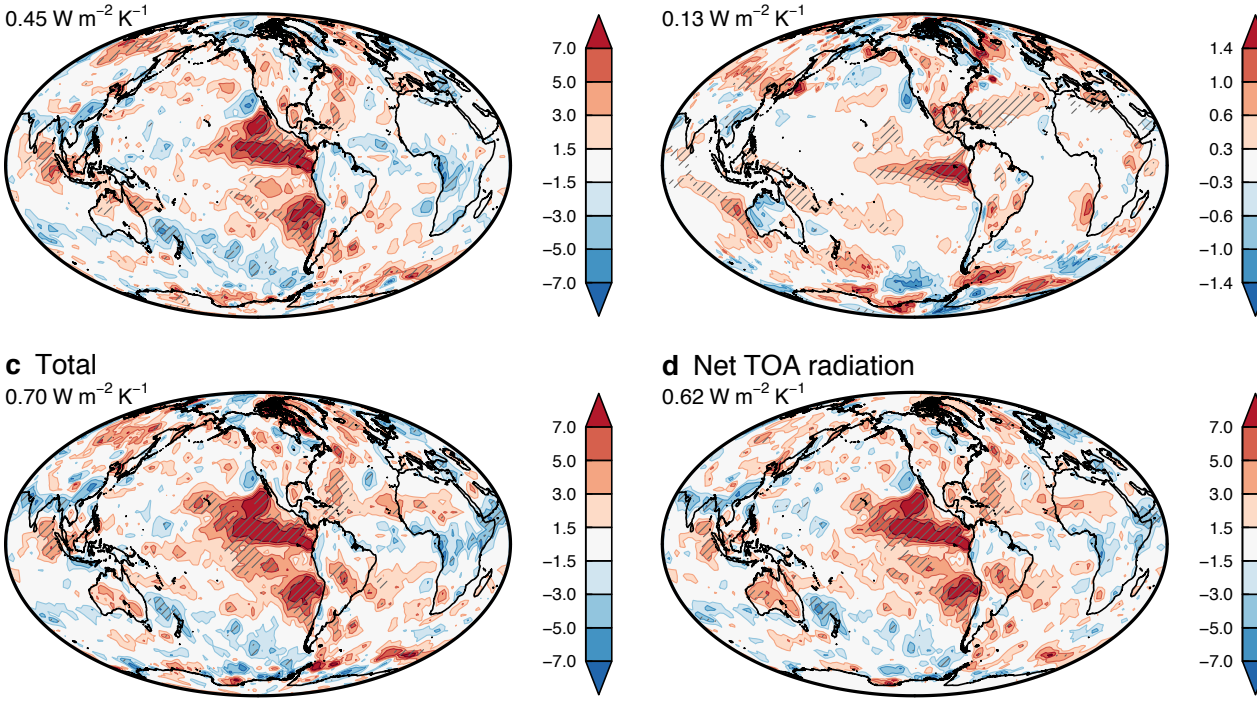

Fig. S6. Contributions to stability-induced top-of-atmosphere radiative anomalies in observations by (a) clouds, (b) lapse rate changes, and (c) the sum of all the components (Planck, lapse rate, water vapor, surface albedo, and clouds). Panel (d) shows the actual net radiative anomalies (as in Fig. 4d) for comparison with (c). The radiative anomaly decomposition in (a)–(c) was calculated with radiative kernels (Materials and Methods). All the anomalies are scaled for a -0.16 K K^{-1} change in global-mean EIS for comparison with climate model results (cf. main text and Fig. 4). Hatching indicates a statistically significant regression coefficient at the 5% level.

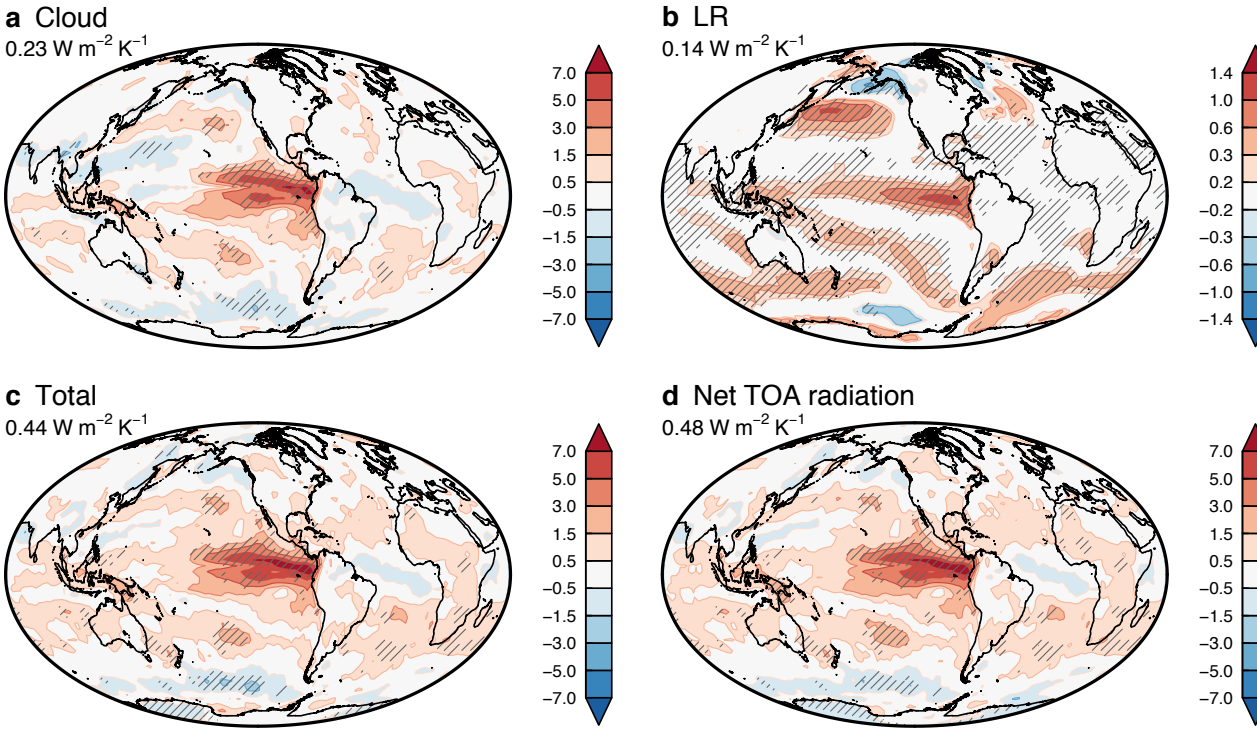

Fig. S7. As in Fig. S6, but for the interannual stability-induced radiative anomalies in climate models (cf. Fig. S5). Shading represents multi-model mean results, and hatching denotes a multi-model mean anomaly larger than one standard deviation across models.